Supporting Information

Two-Photon Nanolithography of Tailored Hollow three-dimensional Microdevices for Biosystems

Caizhi Liao[†], *Will Anderson*[*†], *Fiach Antaw*[†], *Matt Trau*[*†‡]

[†] Centre for Personalized Nanomedicine, Australian Institute for Bioengineering and Nanotechnology (AIBN), The University of Queensland, Corner College and Cooper Roads (Bldg 75), Brisbane QLD 4072, Australia

‡ School of Chemistry and Molecular Biosciences, The University of Queensland, Brisbane QLD 4072, Australia

Dr. W. Anderson Email: will.anderson@uqconnect.edu.au

Prof. M. Trau Email: m.trau@uq.edu.au

Contents

Figures:

Tables:

Video S1: Real-time DLW-TPP fabrication of hollow 3D microstructures

Video S2: Current trace curve of nanoparticles translocate through hollow micropore.

Video S3: Confocal rotational images of 3D hollow microstructures

1. Introduction

1.1 Two-photon Polymerization (TPP) Mechanism

In 1931, Maria Goeppert-Mayer theoretically described the process of two-photon adsorption (TPA), in which interactions between two photons and one atom/molecule take place during a single quantum event[S1]. As an essential part of TPA process, the collective action of two photons must be present simultaneously to impart enough energy to induce the transition[S2] (See **Figure 1b**). To obtain nano/micro-objects with high spatial resolution by making use of TPA polymerization, efficient emission by photosensitiseris of significant importance[S3-4].When a high intensity laser pulse beam is precisely focused into the small focal volume of photosensitive material, the photosensitiser chromophore is excited by the simultaneous absorption of two photons and emits fluorescent light in the UV-*vis* regime, which is generally used to enhance two-photon activation. Photoinitiators with high photochemical activity then absorb the emitted fluorescent light and generate radicals (*Initiation*). The radicals serve as the activator react with monomers or oligomers, producing monomer radicals to expand in a chain reaction (*Propagation*) until two radicals meet (*Termination*)[S5-6]. The TPP procedure can be described as follows:

Initiation: $$S \xrightarrow{h\nu, h\nu} S^* \xrightarrow{FL} \xrightarrow{I} I^* \xrightarrow{R} R^\bullet$$

Propagation: $$R^\bullet + M \longrightarrow RM^\bullet \xrightarrow{M} RMM^\bullet \cdots\cdots\cdots \xrightarrow{M} RM_n^\bullet$$

Termination: $$RM_n^\bullet + RM_m^\bullet \longrightarrow RM_{n+m}\ R$$

in which *S* is photosensitiser, *I* is photoinitiator, *M* is monomer, and $R^\bullet$ is active radicals. S^* and I^* represent the excited state of photosensitiser and photoinitiator, respectively. $h\nu$ is the Planck's Equation energy for each adsorbed photon, and *FL* is the fluorescent light emitted by the excited state photosensitiser.

1.2 Resistive-pulse Analysis

Resistive-pulse sensing (RPS) is an experimental technique used to characterize colloidal particles ranging from approximately 50 nm in diameter up to the size of cells. Resistive pulse sensing can trace its origins back to the Coulter counter, which was proposed in the late 1940s to count and size biological cells and microorganisms[S7-8]. RPS has enabled high throughput micro-particle-by-particle and cells analysis since the 1950s, submicron particles including viruses since the 1970s, particles as small as single molecules over the past decades, and has inspired a particularly intense interest in nanohole-based DNA sequencing analysis recently[S9-11].

To set up the resistive-pulse sensing system, two reservoirs separated by a hole structure are filled with electrolytes (**Figure 5b** and **Figure S10**). In measurement, the resistance of hole is monitored by applying a voltage between the reservoirs, which drives a flux of electrolyte ions through it and detecting a current flowing from the voltage source. Transient ionic current changes caused by the translocation of analytes through the hole structure are denoted as "blockade events", whose magnitude is closely related to the analyte properties[S12]. As shown in *eqns* (1) and (2), where ρ is the resistivity of electrolyte, d is the analytes diameter and D is the hole diameter, the magnitude of current blockade increases significantly as the analytes expand the size.

$$\Delta R = \frac{4\rho d^3}{\pi D^4} \qquad (1)$$

$$\Delta i(\%) = \frac{\Delta R}{\Delta R + R} \approx \frac{\Delta R}{R} \qquad (2)$$

To date, a plethora of opening hole structures have been investigated for RPS analysis, including solid-state holes (*e.g.*, silicon-based membranes) *via* photolithographic etching, protein holes (*e.g.* α-hemolysin) *via* self-assembly and polymer holes (*e.g.*, PET) *via* track etching[S13]. The breadth of this field can be inferred by the utilization of varied hole materials including carbon nanotubes, micropipettes, silicon nitride and polymer materials, as well as the diverse techniques for hole fabrication, such as ion beam sculpting, track etching, laser melting, electron beam and soft lithography. However, absolute control over the 3D geometric features of hole structures still remains a significant challenge for conventional fabrication techniques.

2. Experimental Methods

2.1 Development Process for 3D Hollow Microstructures

After DLW process, organic solvents were used to fully remove the unexposed, uncross-linked photoresist materials both trapped inside and anchored outside the 3D hollow microstructures[S14] (**Figure S2a**). Corresponding organic solvents development systems for each type of investigated photoresist were listed in **Table S2.** Determining factors affecting the development process, including development time, opening hole size and interior hollow volume, were experimentally explored and are comprehensively discussed. One significant parameter affecting the opening quality is the development time. As shown in **Figure S2b,** it needs at least 12 hrs to completely develop the hollow micropore structure with a 3 μm-sized circular opening. As the opening size was increased, the minimum required time to finish the development process was dramatically decreased (**Figure S2c**). The built-in opening components play a crucial role in the formulation of interior hollow components and facilitate the wash-away process of the un-reacted resist material trapped inside the hollow part (Green-circled area). Since the volume of the hollow part was fixed, the uncross-linked resist materials trapped inside could be fully removed within a shorter period of time when the opening size was increased, thus correspondingly reduce the minimum required development time (*e.g.,* 1μm-sized opening: **24 hrs** *vs* 6 μm-sized opening: **6 hrs**).

Additionally, it has been shown that when the opening size was fixed, the minimum required development time to obtain workable 3D hollow microstructures would be linearly increased with the volume size of the hollow part (**Figure S2d**). For instance, when the volume size of hollow part was small (~4×10^5 μm^3) , the minimum required development (T_{Min}) was around 9 hrs. As the hollow part was increased to 13×10^5 μm^3, the T_{Min} increased to 28 hrs

correspondingly. For the hollow microstructures, the amount of unreacted resist material trapped inside increased correspondingly as the volume size of the hollow part was enlarged. Therefore, to fully remove the uncross-linked resist materials for the microstructures with a larger-sized hollow part, the minimum required development time would be increased. This study on the post-development aspects provides significant insight into the precise fabrication of tailored 3D hollow microstructures with accurately defined hollow components.

2.2 Laser Ablation of Substrate Microhole for 3D Hollow Micropore

The 3D hollow micropore structure used for resistive-pulse analysis was assembled on the plastic PET substrate. To realize the resistive-pulse analysis function of the micropore system, substrate hole (Ø~100 μm) beneath the hollow micropore structure was firstly created using our proposed laser ablation technique. To start with, the plastic PET substrate (7 Mil thick, with protective film on both sides) was cleaned by 5 mins ultrasonic treatment. The cleaned plastic substrate was then mounted onto the Nanoscribe-controlled *XYZ* piezo stage. The 3D ablation process was performed using the laser pulses generated by a mode-locked Ti: sapphire femtosecond laser system (780 nm, 80 MHz, 100 fs). The output from the femtosecond laser source had a Gaussian intensity profile that tightly focused within the PET substrate through a 25X objective lens (0.8 NA). To precisely prepare the through cylindrical micro-holes in plastics, a three-step processing scheme (two FAST ablation steps plus one SLOW polish step) was performed.

In laser ablation process, the input fluence level was set to 0.4 $J \cdot cm^{-2}$, the scanning speed was at 70 k μm/s. **Figure S9** shows the micro-hole structure (Ø: 100 μm) fabricated by the laser ablation technique. The micro-hole has sharp edges and a clean sidewall, without any

observable non-defined bulges that would indicate the re-solidification of heat-induced melting debris that form in classical laser ablation processes. After the micro-hole fabrication in PET substrate, we then dropped the photoresist (~80 µL) to fully cover the laser ablated micro-hole. With the aid the incorporated CCD camera, the initial direct-writing position was aligned with the central position of ablated micro-hole. After this, the processed .STL file containing geometric information of the 3D hollow micropore structure was imported into the Nanoscribe system for the direct laser writing process.

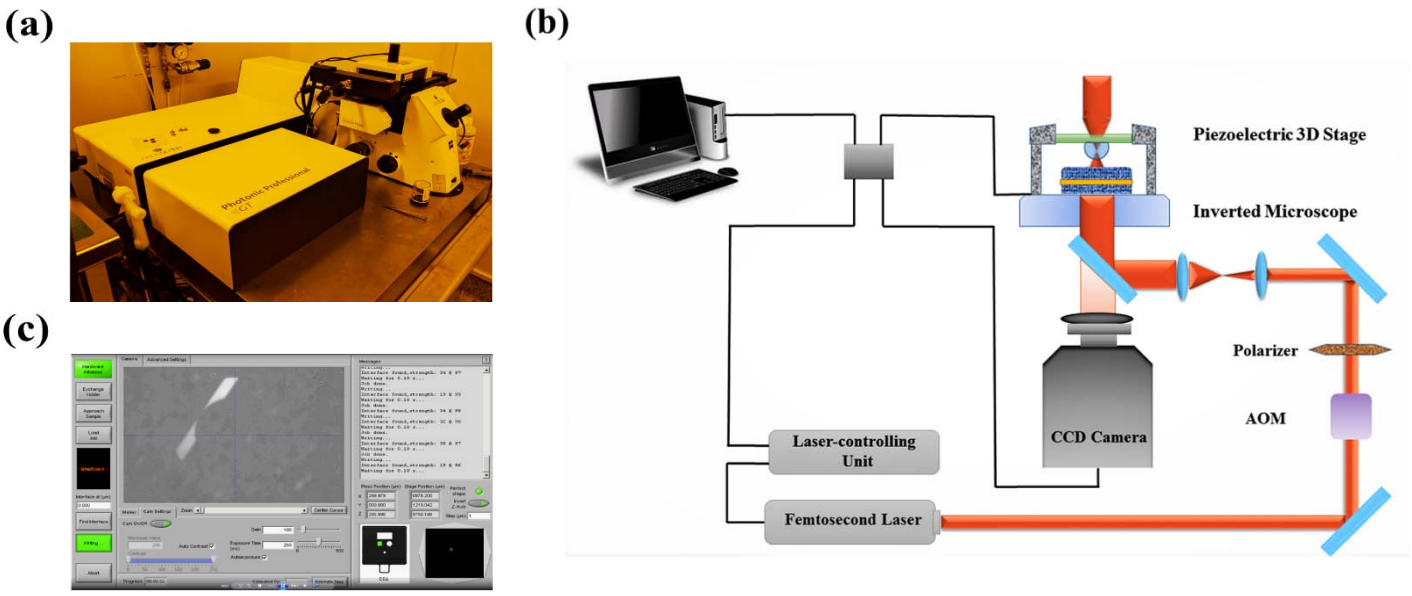

Figure S1. Setting-up of the Nanoscribe system. (a) Picture of the Nanoscribe Photonic Professional GT system. (b) Scematic graph of Nanoscribe system setting-up, most importantly including a femtosecond laser source, a CCD camera and a piezoelectric 3D stage. (c) Interface of the Nanowrite program controlling the direct laser writing of 3D hollow microstructures.

Table S1. Minimum required development time for openings with distinct geometric shapes

Opening Shape	Triangle	Rectangle	Pentagon	Hexagon	Star
Minimum Development Time	~18 hrs	~16 hrs	~16 hrs	~15 hrs	~24 hrs
Dynamic Laser Power Range	50%~60%	50%~60%	50%~60%	50%~60%	50%~60%

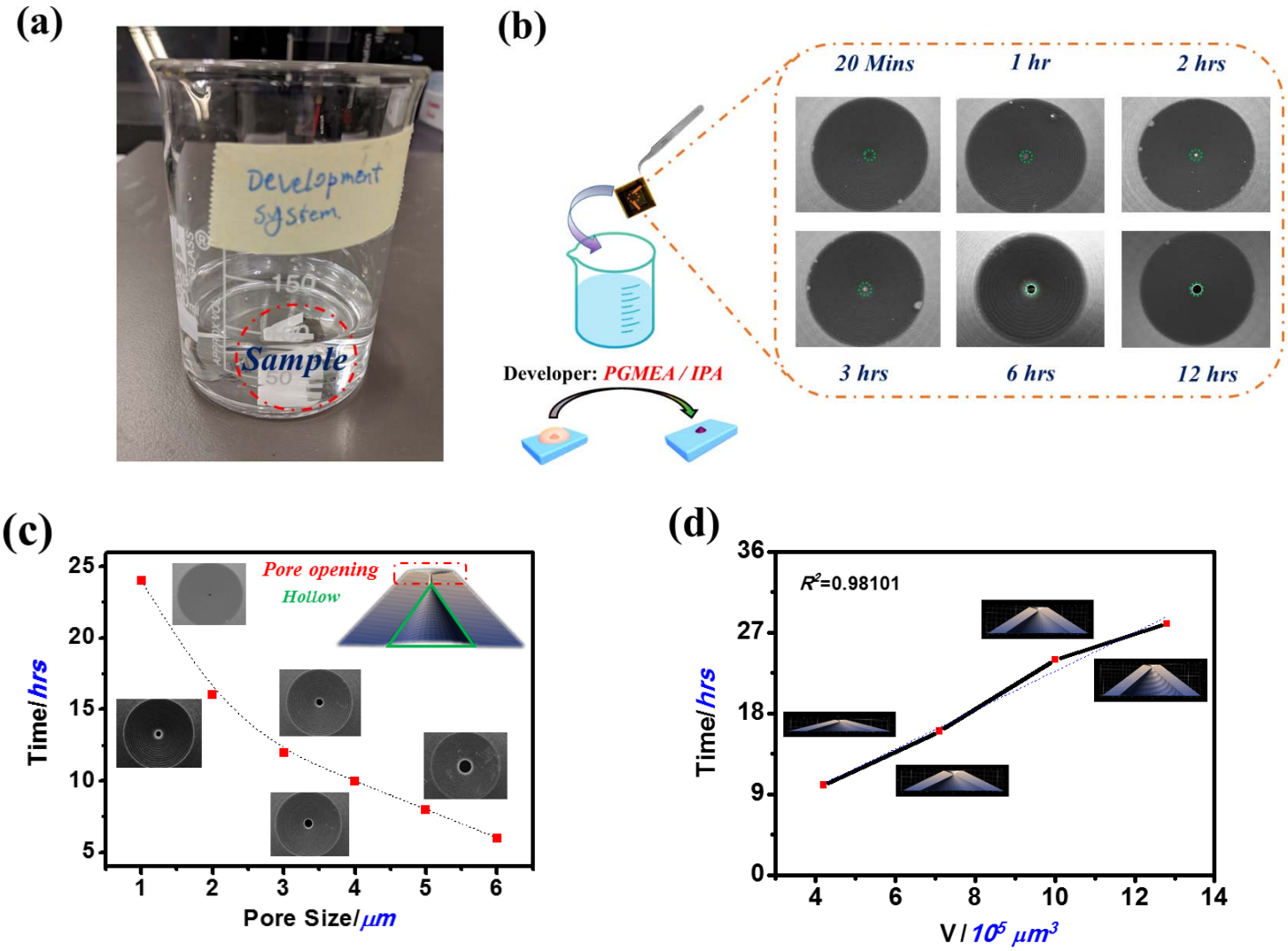

Figure S2. (a) Optical image of the development system used to removed the uncross-linked resist materials. (b) The effects of development time on the morphological quality of the circular opening structure (3μm). (c) Minimum development time required to fully remove uncross-linked resist materials *vs* the opening size. (d) Minimum development time required to fully remove uncross-linked resist materials *vs* the 3D inside hollow volume size.

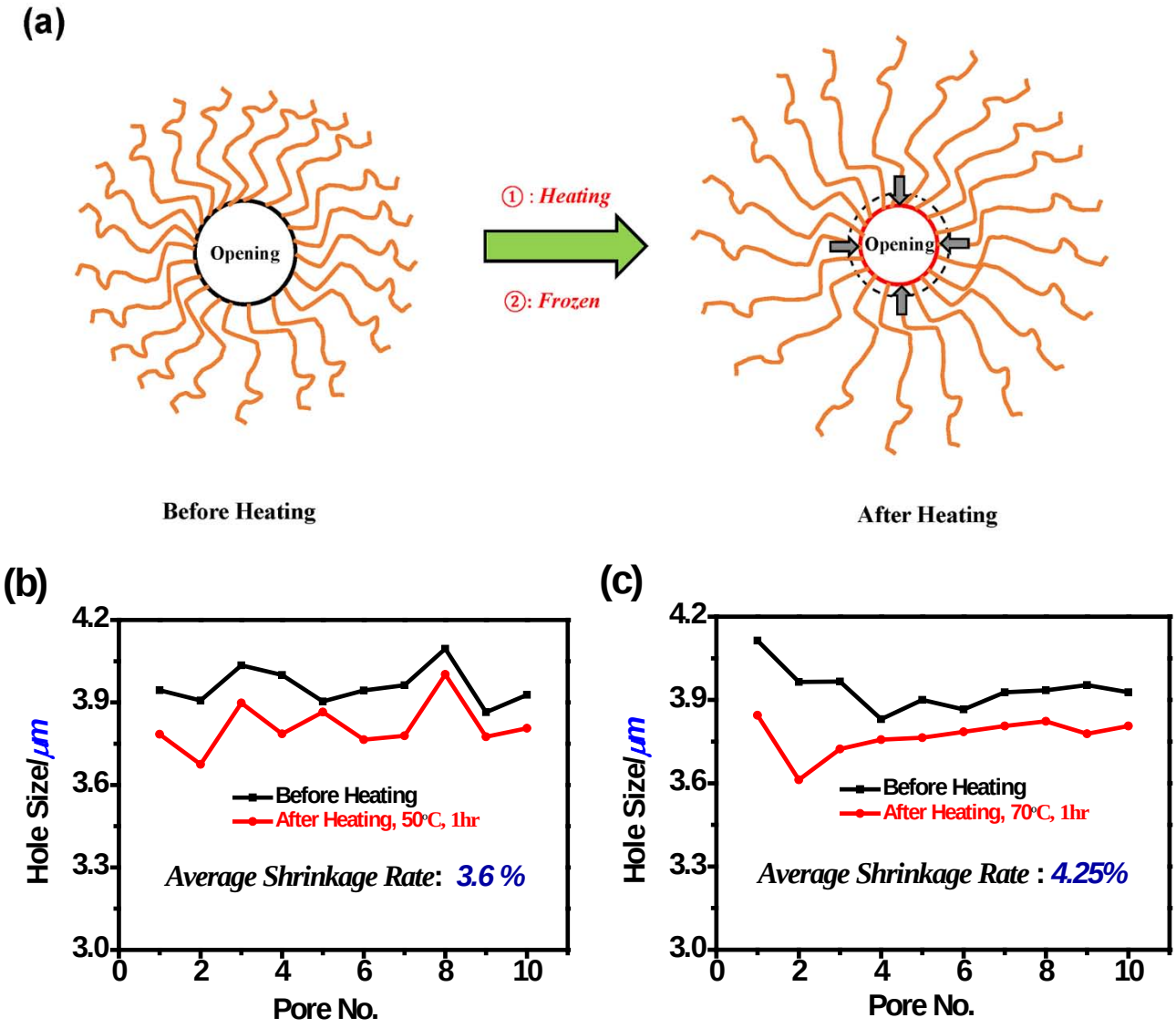

Figure S3. (a) Schematic figure shows the opening part size changes under heating effects . (b) The size of the opening (~4μm) before and after heating treatments, 50°C, 10 samples. (c) The size of the opening (~4μm) before and after heating treatments, 70°C, 10 samples.

Table S2. 3D hollow micropore structures (Circular opening 3um in diameter) prepared using different types of photoresists and processing conditions. These structures show good biocompatibility.

Photoresist	SU-8	IP-L	IP-S	IP-Dip	Ormocer
Threshold Energy Level	30 %	40%	40%	30%	50%
Developer Solution	SU-8 Developer	PGMEA/IPA	PGMEA/IPA	PGMEA/IPA	Ormo Developer
Development Time	6 hrs	20 hrs	16 hrs	20 hrs	10 hrs
Biocompatibility	Excellent[S15]	Excellent[S16]	Good[S17]	Good[S18]	Excellent[S19]

Table S3. Tunable surface conductivity of the hollow microelectrode structure. Pt conducting layer was uniformly coated using a metal material sputtering system. The distance between two measured points: ~ 1cm

Coating Time	0s	30s	1 Mins	2 Mins	3 Mins
Pt Layer Thickness	/	~10 nm	~ 20 nm	~ 40 nm	~ 60 nm
Resistivity	+∞	~50 kΩ	~30 kΩ	~16 kΩ	~10 kΩ

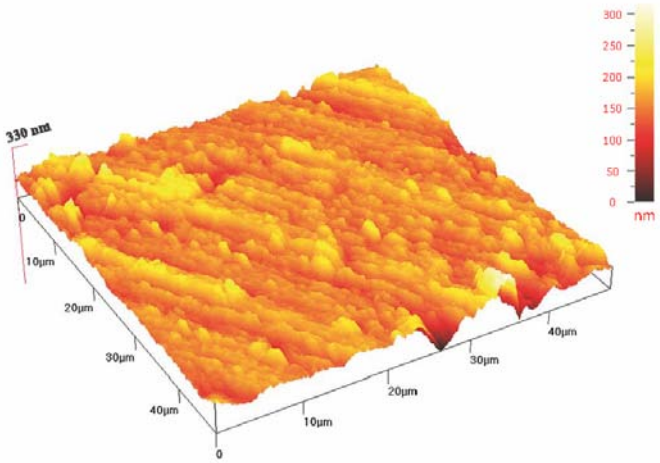

Figure S4. AFM characterization of the surface roughness of the hollow micro-needle surface coated with Pt film (Thickness: ~50 nm)

Table S4. Processing conditions for the preparation of demonstrated 3D hollow biomicrosystem deviecs

Microstructure	Mironeedle-1	Mironeedle-2	Microelectrode	Micropump	Microrobot
Printing Time (***Mins***)	5.5	6.0	5.5	8.5	4.0
Development Time (***Hrs***)	16	18	16	24	12

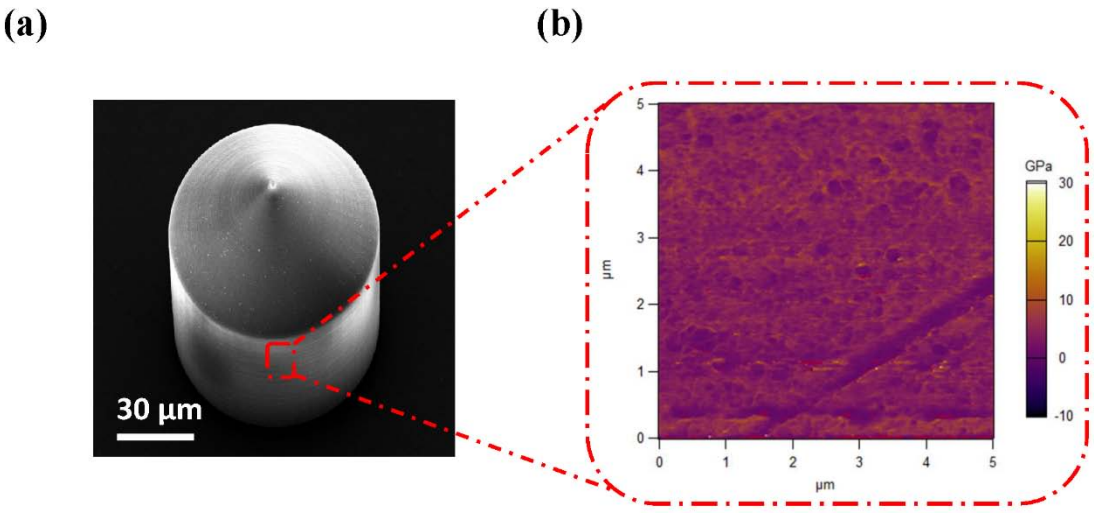

Figure S5. Mechanical properties about 3D hollow microneedle structure. The average Young's Modulus (E_{Young}) was 3.0 ± 0.7 GPa, measured by the AM-FM viscoelastic mapping mode using the Asylum Research MFP-3D-Bio Inverted Optical AFM.

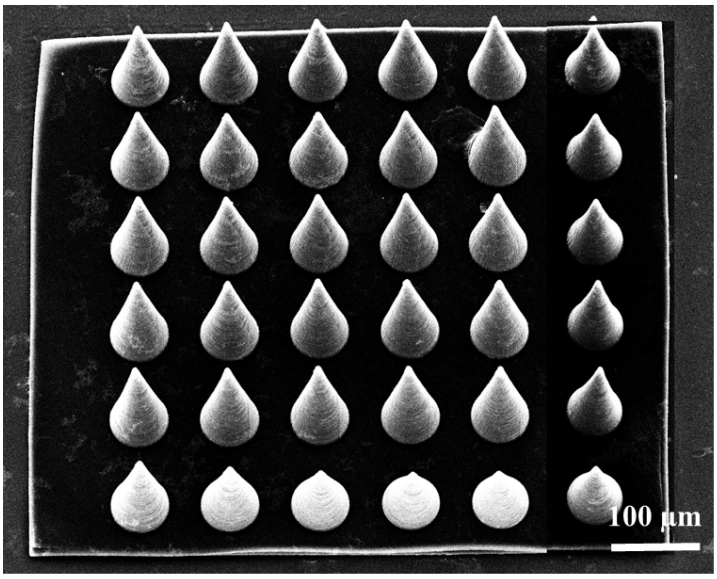

Figure S6. Manipulable microneedle array structure, prepared using IP-S photoresist. Fluence level: 50%, scanning speed: 50k µm/s.

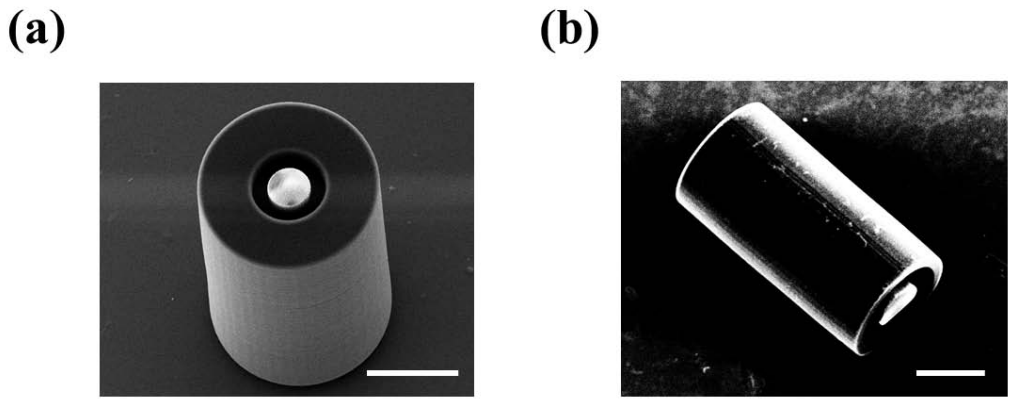

Figure S7. Ultrosonic treatment (~1 min) to detach individual 3D hollow microstructure from the substrate. Micro-valve structure attached on the substrate (a) and detached from the substrate after sonication (b). Scale bar: 80 µm.

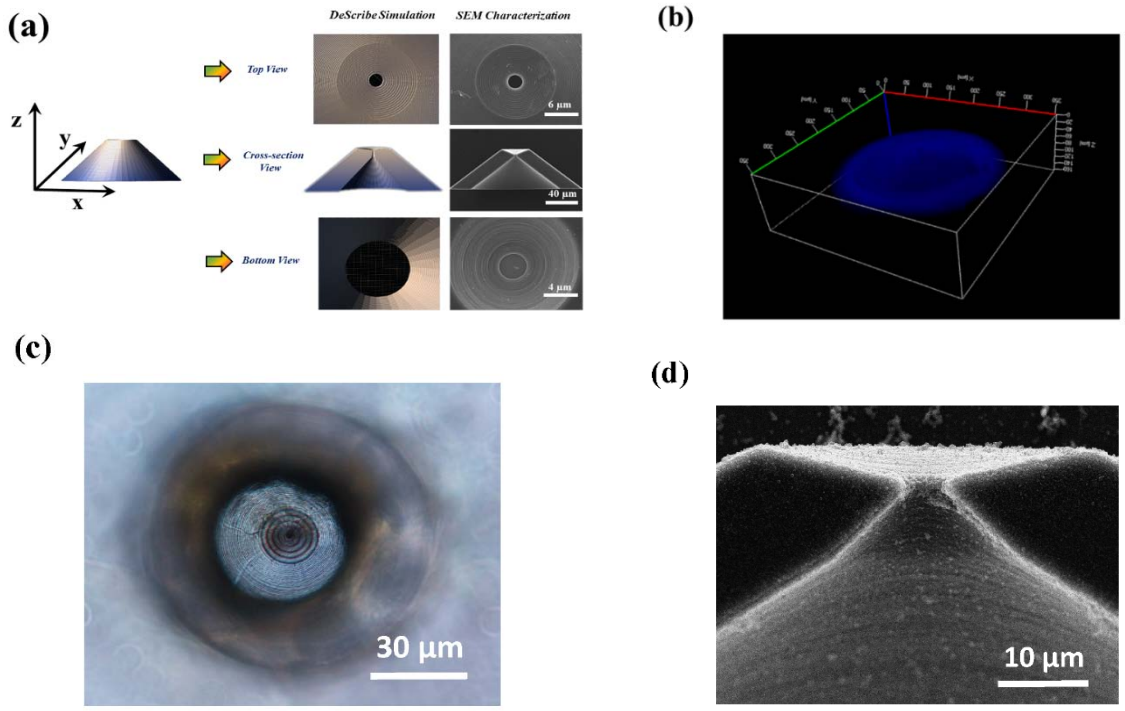

Figure S8. Charactriztions of developed hollow structures (a) Top-view, cross-section view and bottom-up view of 3D hollow micro-devices used for resistive-pulse analysis. Left and middle: Describe simulated structural images; Right: Experimental SEM images. (b) Confocal image of hollow 3D micropore structure. (c) Optical characterization of interial hollow. (c) SEM characterization of half-cut 3D hollow microstructures.

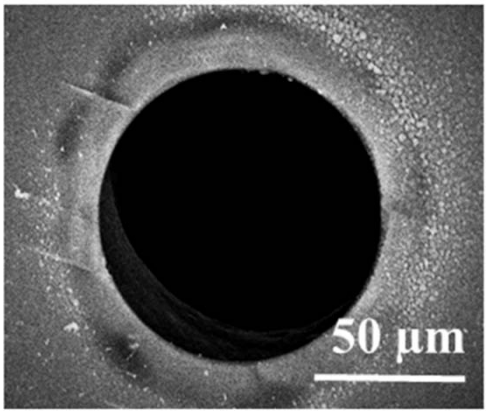

Figure S9. SEM characterization of the laser-ablated micro-hole in the 7 Mil thick PET sbustrate.

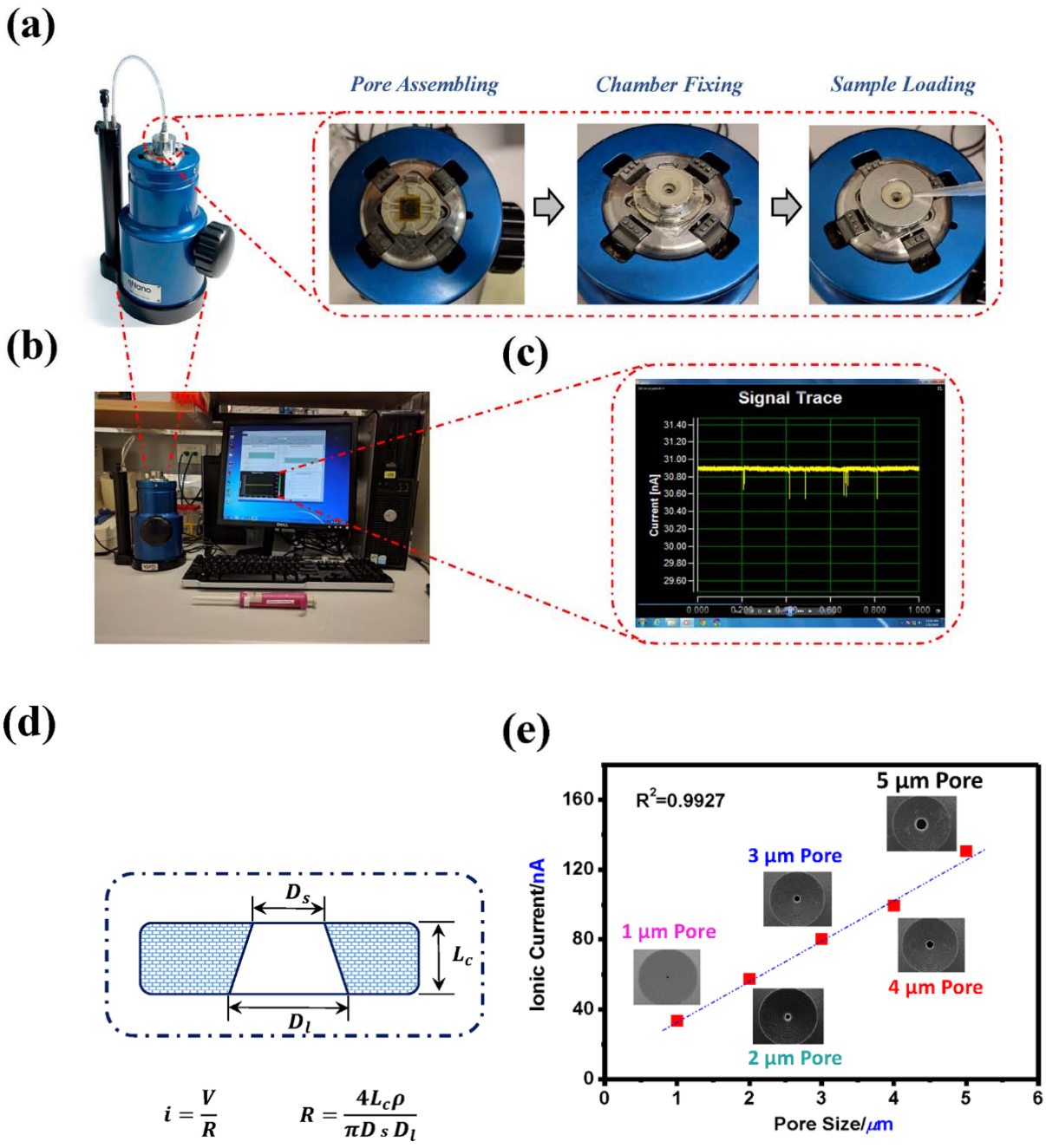

Figure S10. (a) System setting up for the resistive-pulse analysis process. (b) Picture of the resistive-pulse sensing system. (c) Screen capture of the tracking current blockades. (d) Schematic diagram of the conical-shaped micro-cone structure. (e) The magnitude of ionic current *vs* the size of opening hole. Working voltage: 1V.

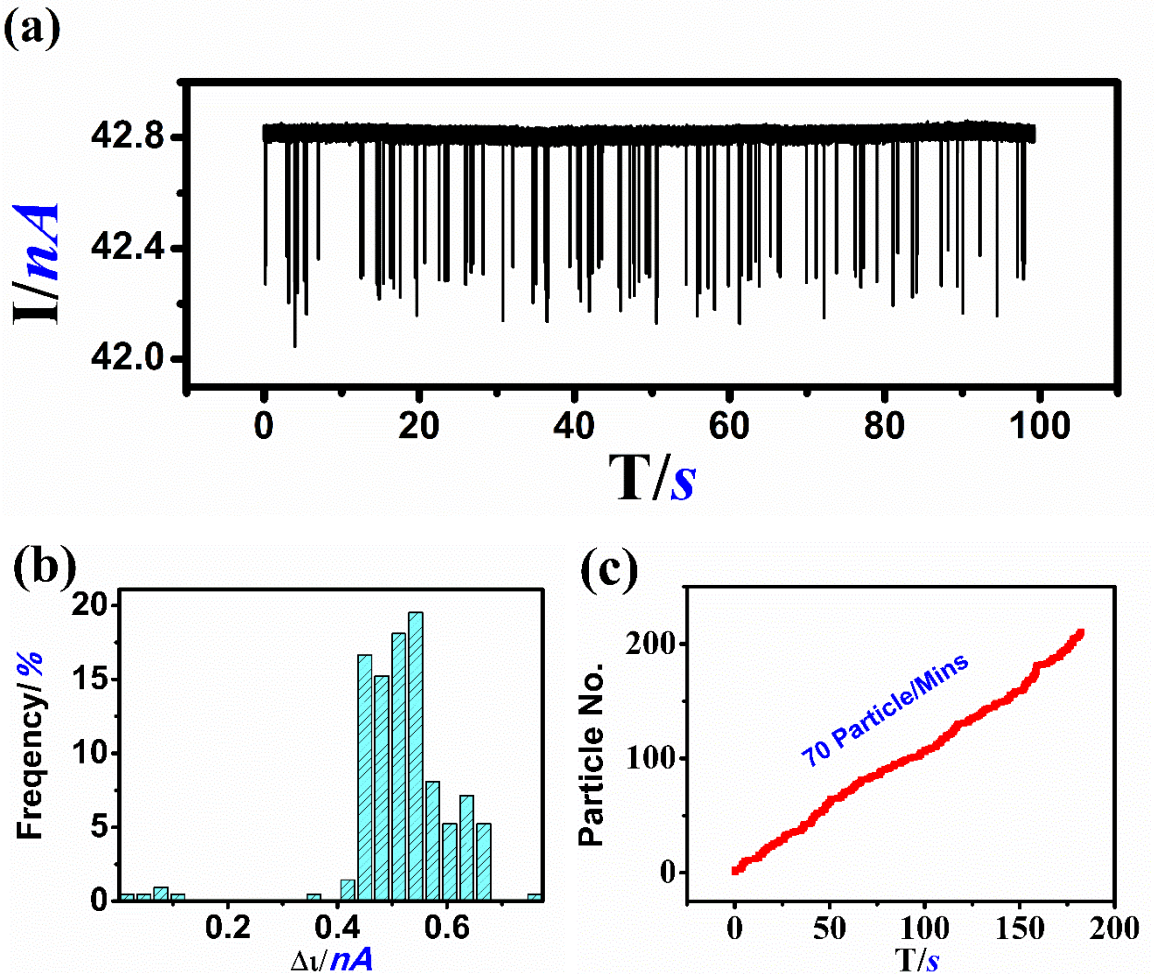

Figure S11. (a) The overall current tracking curve the resistive-pulse analysis of 330 nm PS nanoparticles, using the DLW fabricated 3D hollow micropore structures with 3μm-sized opening. Each current blockade represents each individual nanoparticle translocate throught the hollow strucutre. (b) The magnitude distribution of the current blockades of the 330 nm PS nanoparticles resistive-pulse analysis using the 3D hollow micropore structures with 3μm-sized opening. Working voltage: 0.3V. (c) Rate plot of the 330 nm PS nanoparticles resistive-pulse analysis, with a passing speed at 70 nanoparticles/min with 0.3V applied.

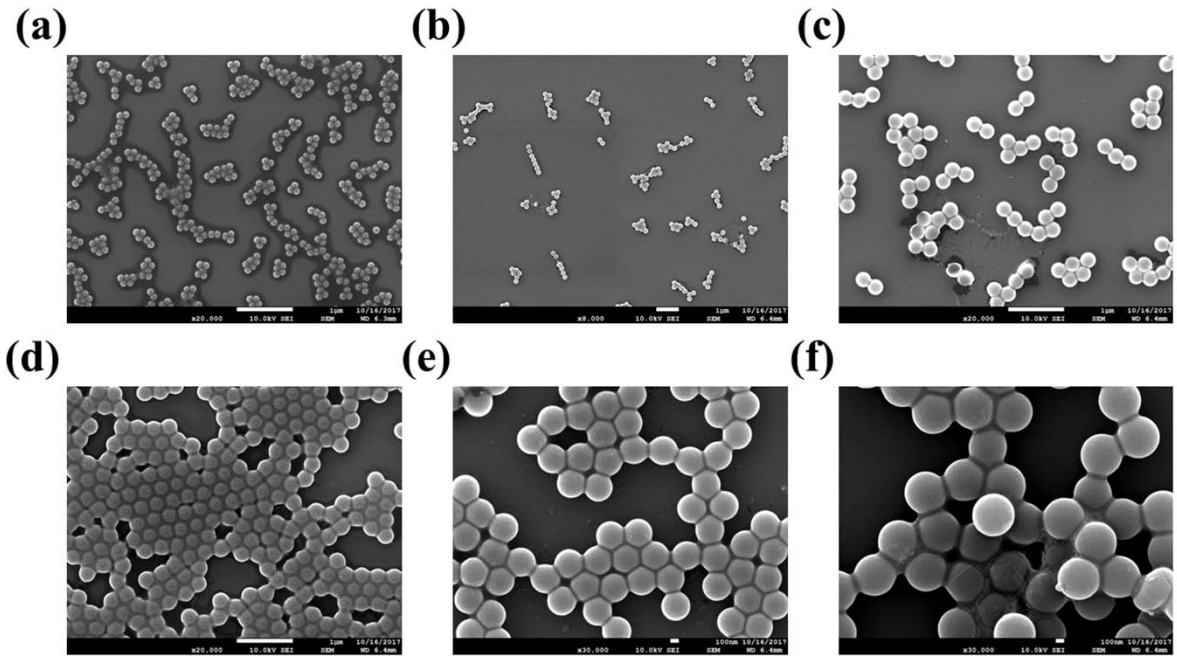

Figure S12. SEM characterization image of different-sized PS nanoparticles. (a) to (f), correspond to 114 nm nanoparticle, 210 nm nanoparticle, 300 nm nanoparticle, 330 nm nanoparticle, 400 nm nanoparticle and 530 nm nanoparticle, respectively.

Table S5. Volume size for each type nanoparticle and recorded magnitude of corresponding current blockade (Mode value) for each individual measurement.

Nanoparticle	**114 nm**	**210 nm**	**300 nm**	**330 nm**	**400 nm**	**530 nm**
Volume/$10^{-3}\mu m^3$	0.775	4.86	14.14	18.82	33.52	77.96
Ionic blockade (Modal) /*nA*	0.061	0.22	0.396	0.534	0.805	1.97

Reference

[S1] Kaiser, W.; Garrett, C. G. B. Two-photon excitation in CaF_2: Eu^{2+} *Phys. Rev. Lett.* **1961**, *7*, 229-231.

[S2] Bray, R. G.; Hochstrasser, R. M. Two-photon absorption by rotating diatomic molecules. *Mol. Phys.* **1976**, *31*, 1199-1211.

[S3] He, G. S.; Xu, C.; Prasad, P. N.; Reinhardt, B. A.; Bhatt, J. C.; McKellar, R.; Dillard, A. G. Two-photon absorption and optical-limiting properties of novel organic compounds. *Opt. Lett.* **1995**, *20*, 435-437.

[S4] Kogej, T.; Beljonne, D.; Meyers, F.; Perry, J.W.; Marder, S.R.; Brédas, J. L. Mechanisms for enhancement of two-photon absorption in donor–acceptor conjugated chromophores. *Chem. Phys. Lett.* **1998**, *298*, 1-6.

[S5] Zhou, W.; Kuebler, S. M.; Braun, K. L.; Yu, T.Y.; Cammack, J. K.; Ober, C. K.; Perry, J. W.; Marder, S. R. An efficient two-photon-generated photoacid applied to positive-tone 3D microfabrication. *Science* **2002**, *296*, 1106-1109.

[S6] Das, S.; Nag, A.; Goswami, D.; Bharadwaj, P. K. Zinc(II)- and copper(I)-mediated large two-photon absorption cross sections in a bis-cinnamaldiminato schiff base. *J. Am. Chem. Soc.* **2006**, *128*, 402-403.

[S7] Kozak, D.; Anderson, W.; Vogel, R.; Trau, M. Advances in resistive pulse sensors: Devices bridging the void between molecular and microscopic detection. *Nano Today* **2011**, *6*, 531-545.

[S8] Blundell, E. L. C. J.; Mayne, L. J.; Billinge, E. R.; Platt, M. Emergence of tunable resistive pulse sensing as a biosensor. *Anal. Methods* **2015**, *7*, 7055-7066.

[S9] Platt, M.; Willmott, G. R.; Lee, G. U. Resistive pulse sensing of analyte-induced multicomponent rod aggregation using tunable pores. *Small* **2012**, *8*, 2436-2444.

[S10] Billinge, E. R.; Broom, M.; Platt, M. Monitoring aptamer–protein interactions using tunable resistive pulse sensing. *Anal. Chem.* **2014**, *86*, 1030-1037.

[S11] Billinge, E. R.; Platt, M. Aptamer based dispersion assay using tunable resistive pulse sensing (TRPS). *Anal. Methods* **2015**, *7*, 8534-8538.

[S12] Kozak, D.; Kithva, P.; Bax, J.; Surawski, P. P.; Monteiro, M. J.; Trau, M. Development of encoded particle-polymer arrays for the accelerated screening of antifouling layers. *Chem Commun (Camb)* **2011**, *47*, 9687-9689.

[S13] Willmott, G. R.; Vogel, R.; Yu, S. S.; Groenewegen, L. G.; Roberts, G. S.; Kozak, D.; Anderson, W.; Trau, M. Use of tunable nanopore blockade rates to investigate colloidal dispersions. *J. Phys. Condens. Matter*. **2010**, *22*, 454116.

[S14] Lee, S. H.; Jeong, H. E.; Park, M. C.; Hur, J. Y.; Cho, H. S.; Park, S. H.; Suh, K. Y. Fabrication of hollow polymeric microstructures for shear-protecting cell-containers. *Adv. Mater*. **2008**, *20*, 788-792.

[S15] Nemani, K. V.; Moodie, K. L.; Brennick, J. B.; Su, A.; Gimi, B. *In vitro* and *in vivo* evaluation of SU-8 biocompatibility. *Mater. Sci. Eng. C Mater. Biol. Appl.* **2013**, *33*, 4453-4459.

[S16] Tottori, S.; Zhang, L.; Qiu, F.; Krawczyk, K. K.; Franco-Obregon, A.; Nelson, B. J. Magnetic helical micromachines: fabrication, controlled swimming, and cargo transport. *Adv. Mater*. **2012**, *24*, 811-816.

[S17] Worthington, K. S.; Wiley, L. A.; Kaalberg, E. E.; Collins, M. M.; Mullins, R. F.; Stone, E. M.; Tucker, B. A. Two-photon polymerization for production of human iPSC-derived retinal cell grafts. *Acta. Biomater.* **2017**, *55*, 385-395.

[S18] Hengsbach, S.; Lantada, A. D. Rapid prototyping of multi-scale biomedical microdevices by combining additive manufacturing technologies. *Biomed. Microdevices* **2014**, *16*, 617-627.

[S19] Haas, K.H.; Wolter, H. Synthesis, properties and applications of inorganic–organic copolymers (ORMOCER®s). *Curr. Opin. Solid State Mater. Sci.* **1999**, *4*, 571-580.